J. Fluid Mech. (1984), *vol.* 141, *pp.* 67–95
Printed in Great Britain

Rotating flow past disks and cylindrical depressions

By DON L. BOYER,
Department of Mechanical Engineering, University of Wyoming, Laramie, Wyoming 82071, USA

PETER A. DAVIES
Department of Civil Engineering, The University, Dundee DD1 4HH, UK

AND WILLIAM R. HOLLAND
National Center for Atmospheric Research, P.O. Box 3000, Boulder, Colorado 80307, USA

(Received 18 October 1982 and in revised form 21 November 1983)

The flow of a rotating fluid over isolated three-dimensional topographic features has been investigated. Laboratory experiments have been conducted with a rotating water channel to determine the characteristics of the flow over and around truncated cylindrical disks and depressions located on the upper and lower bounding surfaces of the channel. The geometry of the rotating channel allowed the beta effect to be modelled and cases of beta-plane westward, beta-plane eastward and f-plane flows were studied. Flow patterns revealed by the use of an electrolytic precipitation technique are presented, and the flow behaviour is quantified in terms of a characteristic speed of the flow through a circular cylinder circumscribing the topography in the vicinity of the channel midplane. Case studies are presented for a range of values of Rossby number, Ekman number, beta parameter, and cylinder height-to-radius ratio. The vorticity equation and associated boundary conditions are discussed for the cases studied in the laboratory and appropriate numerical solutions are obtained. The laboratory and numerical experiments demonstrate the character of the horizontal steering of fluid by the topographic features as a function of the system parameters. Comparisons between laboratory and numerical experiments are presented and shown to be in good agreement.

1. Introduction

In a recent laboratory study two of us (Boyer & Davies 1982) conducted an extensive series of experiments on the flow past a right circular cylinder on a beta-plane; see figure 1 with the obstacle being a 'full cylinder' extending from the lower to the upper surface. This paper will be referred to as BD (1982) in the following. The investigation utilized a horizontal-axis flow channel mounted on a vertical-axis turntable capable of rotating either clockwise or anticlockwise. The upper and lower surfaces of the channel were sloped to simulate the beta-effect with the narrow portion of the channel being toward the north (see figure 1). Eastward and westward beta-plane, as well as f-plane (zero channel slope), flows could thus be investigated. The working fluid was water and the resulting characteristic motions were observed utilizing an electrolytic-precipitation flow-visualization technique.

The study demonstrated a number of interesting flow phenomena unique to rotating systems and not heretofore discussed in the literature. For example, it was shown that, for eastward flow on a beta-plane, a region in the near wake of the cylinder

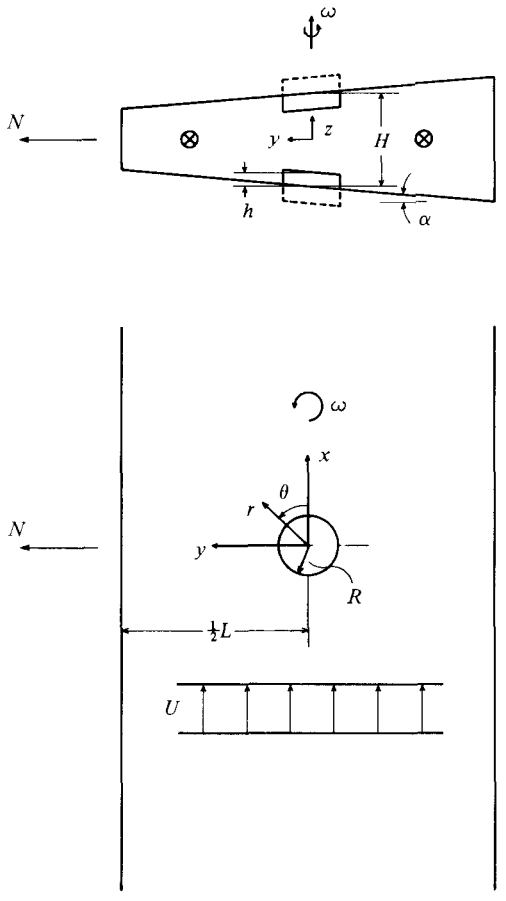

FIGURE 1. Physical system.

existed in which the characteristic speed exceeded that of the freestream. It was also demonstrated that the beta-effect tends to suppress flow separation for eastward flows while enhancing it for westward flows, other parameters being fixed. The investigation was quantitative in the sense that the extent of the separated bubble region downstream of the cylinder was measured as a function of the various system parameters.

The purpose of the present study is to extend the full-cylinder investigation to the flow over isolated steep-sided topographic features of circular form. In the laboratory these take the form of raised disks and cylindrical depressions with vertical sidewalls (see figure 1), while in the numerical experiments these features have steep but finite sidewall slopes.

By dimensional analysis it is easily shown that the physical system depicted in figure 1 is characterized by the following parameters:

(*a*) $Ro = U/2\omega R$, the Rossby number;

(*b*) $E = \nu/2\omega R^2$, the Ekman number;

(*c*) $\beta = \alpha(R/H)/Ro$, a beta-parameter;

(*d*) R/H, the ratio of topography radius to mean channel depth;

(*e*) $2h/H$, twice the ratio of topography height to mean channel depth;

(*f*) L/R, the ratio of channel width to topography radius;

(*g*) eastward or westward, the flow direction for beta-plane motions.

In addition, when the slope of the sidewalls of the topographic feature is finite (in the numerical experiments) it must also be included as a parameter. In the above U is the freestream speed, ω the rotation rate, R the topography radius, ν the kinematic viscosity, α the cross-channel slope, H the channel height, h the height of the topographic feature, W_0 the width of the sloping region (for the numerical experiments), and L the channel width.

In §2 the results of the laboratory programme are presented. The principal aim of this section is to discuss qualitatively the character of the disk and cylindrical-depression flows for the range of dimensionless parameters considered. A further aim is to estimate a characteristic horizontal speed in the circumscribing cylinder as a function of the various system parameters; i.e. a 'Taylor-column speed'. In §3 the quasigeostrophic equations for viscous flow over topography are given, and in §4 numerical techniques for their solution discussed. Section 5 includes the results of various numerical calculations and their comparison to laboratory flows.

2. Laboratory experiments

The experimental apparatus utilized and the technques employed were the same as in the full cylinder study reported in BD (1982). The interested reader is referred to that paper for details.

A principal difficulty in designing a laboratory programme for physical systems such as those being considered here is the large number of parameters required to characterize the flow; the present system involves seven dimensionless parameters. It was thus necessary to focus the experiments on variations in a limited number of the system parameters. In this regard the experimental design was as follows:

$R = 2.54$ cm, $L = 35.6$ cm, $H = 3.49$ cm – all runs;

$h = 0.44, 0.87, 1.31$ cm – disk;

$h = 0.44, 0.87, 1.31, 2.62$ cm – cylindrical depression;

$\omega = 0.5, 1.0, 2.0$ rad/s;

$U = 0.25, 0.50, 1.00$ cm/s;

$\alpha = 0.00, 0.0536$.

This experimental design allowed for the following systematic comparisons of flow behaviour:

(*a*) disk versus cylindrical depression;

(*b*) effect of variation of topographic aspect ratio, other parameters being fixed;

(*c*) effect of flow direction (i.e. eastward or westward) for beta-plane flows;

(*d*) effect of variation of the Rossby number – note that since only one sloped channel was considered for beta-plane flows and that the beta parameter includes the Rossby number, variations in Ro were tied to variations in β, so that effects of β and Ro could not be separated;

(*e*) effect of variation in the Ekman number, other parameters being fixed.

The discussion of the experimental results will be given in two parts. First the qualitative nature of the resulting flows will be considered. Then some measures for quantifying certain flow characteristics will be advanced and the results discussed.

Figures 2 and 3 depict a series of horizontal streamline patterns in the midplane ($z = 0$) of the flow channel for a disk and cylindrical depression respectively. Figures 2(*a*) and 3(*a*) are for f-plane flow (i.e. $\beta = 0$), and the flow is from left to right with

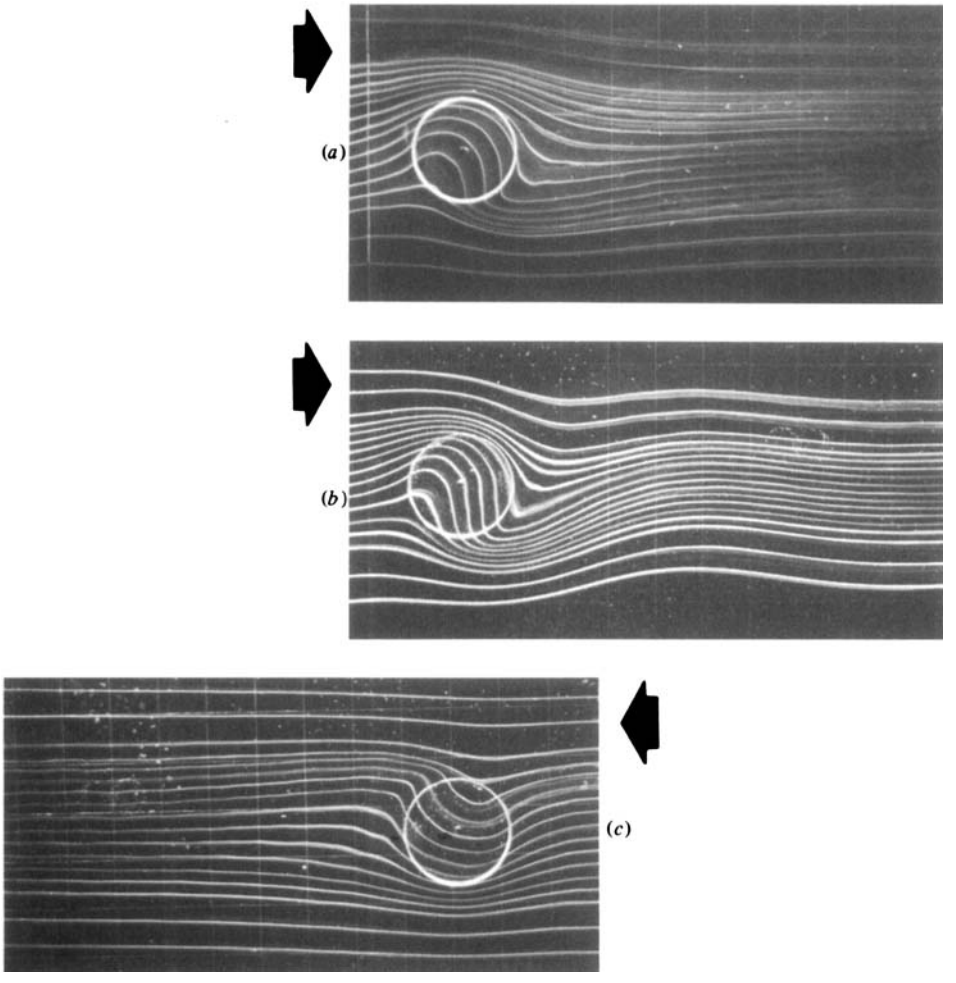

FIGURE 2. Midchannel streaklines; disk; $Ro = 9.8 \times 10^{-2}$, $E = 15.4 \times 10^{-4}$ ($Re = 64$), $2h/H = 0.25$, $R/H = 0.73$: (*a*) *f*-plane (i.e. $\beta = 0$); (*b*) beta-plane eastward ($\beta = 0.40$); (*c*) beta-plane westward ($\beta = 0.40$).

the rotation being anticlockwise. Figures 2(*b*) and 3(*b*) depict eastward flow with the flow being from left to right (i.e. west to east) with north being toward the top and with the rotation being anticlockwise. Figures 2(*c*) and 3(*c*) represent westward flow with the motion being right to left (i.e. east to west) and with north being toward the top and again the rotation anticlockwise.

In comparing the disk with the depression flows it is clear that the motion above the topographic feature is predominantly anticyclonic (relative vorticity of opposite sign to the basic rotation) for the disk and cyclonic (relative vorticity of the same sign as the basic rotation) for the depression. This is a common feature of all experiments conducted.

A second feature of note is that for eastward flows (see figures 2*b*, 3*b*) there is a tendency for the lateral separation of streamlines to be reduced downstream of the topographic feature (either disk or depression). This jetting effect in the wake of the feature is reminiscent of the jetting found in the wake of solid cylinders in eastward

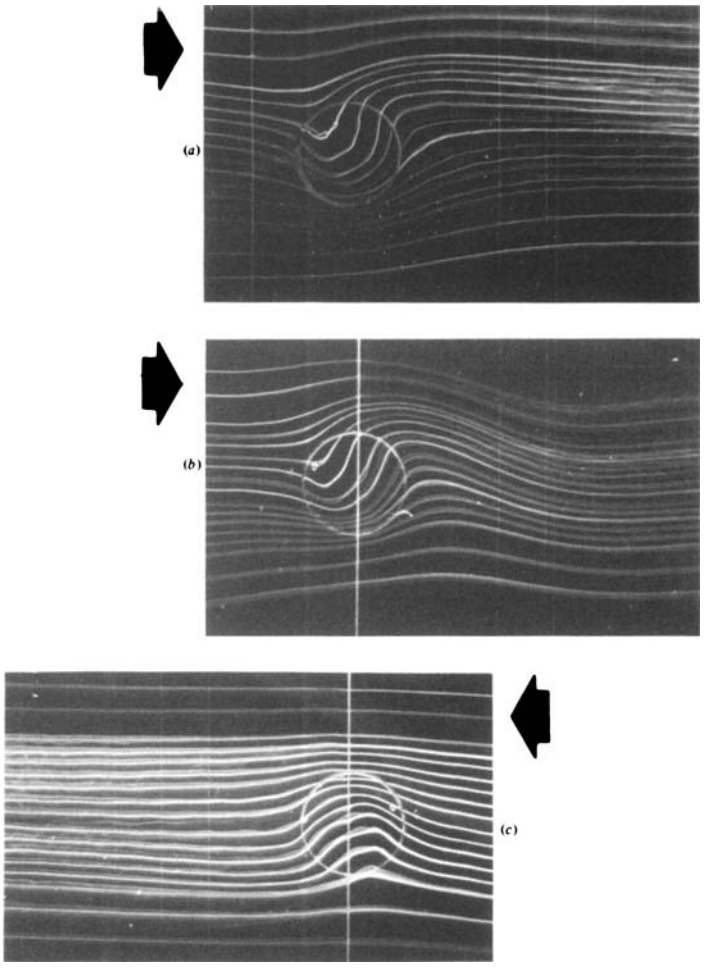

FIGURE 3. Midchannel streaklines; cylindrical depression; $Ro = 9.8 \times 10^{-2}$, $E = 13.8 \times 10^{-4}$ ($Re = 71$), $2h/H = 0.75$, $R/H = 0.73$: (*a*) *f*-plane ($\beta = 0$); (*b*) beta-plane eastward ($\beta = 0.40$); (*c*) beta-plane westward ($\beta = 0.40$).

flow as discussed in BD (1982). One notes also that for eastward flows the streamlines in the wake exhibit a damped Rossby-wave pattern similar to that noted in BD (1982) for a solid cylinder. A major difference here, however, is that these patterns are not symmetric about the freestream axis x as they were for 'almost fully attached flows' in the wake of solid cylinders (see BD 1982).

Beta-plane westward (figures 2*c*, 3*c*) and *f*-plane flows (figures 2*a*, 3*a*) do not exhibit jetting in the wake; this observation again is in consonance with that found for a solid cylinder in BD (1982).

Figures 4 and 5 depict midchannel streamlines for a disk and depression respectively, and demonstrate the importance of the topographic feature aspect ratio. Figure 4 is an eastward flow case with the motion from left to right and the rotation being anticlockwise. It is noted that the disks extend through 0.25, 0.50 and 0.75 of the channel depth in moving from figures 4(*a–c*) respectively. Note that jetting in the wake can be observed for all cases and that the amount of flow passing over the disk decreases dramatically as the disk height increases (as one would expect from the

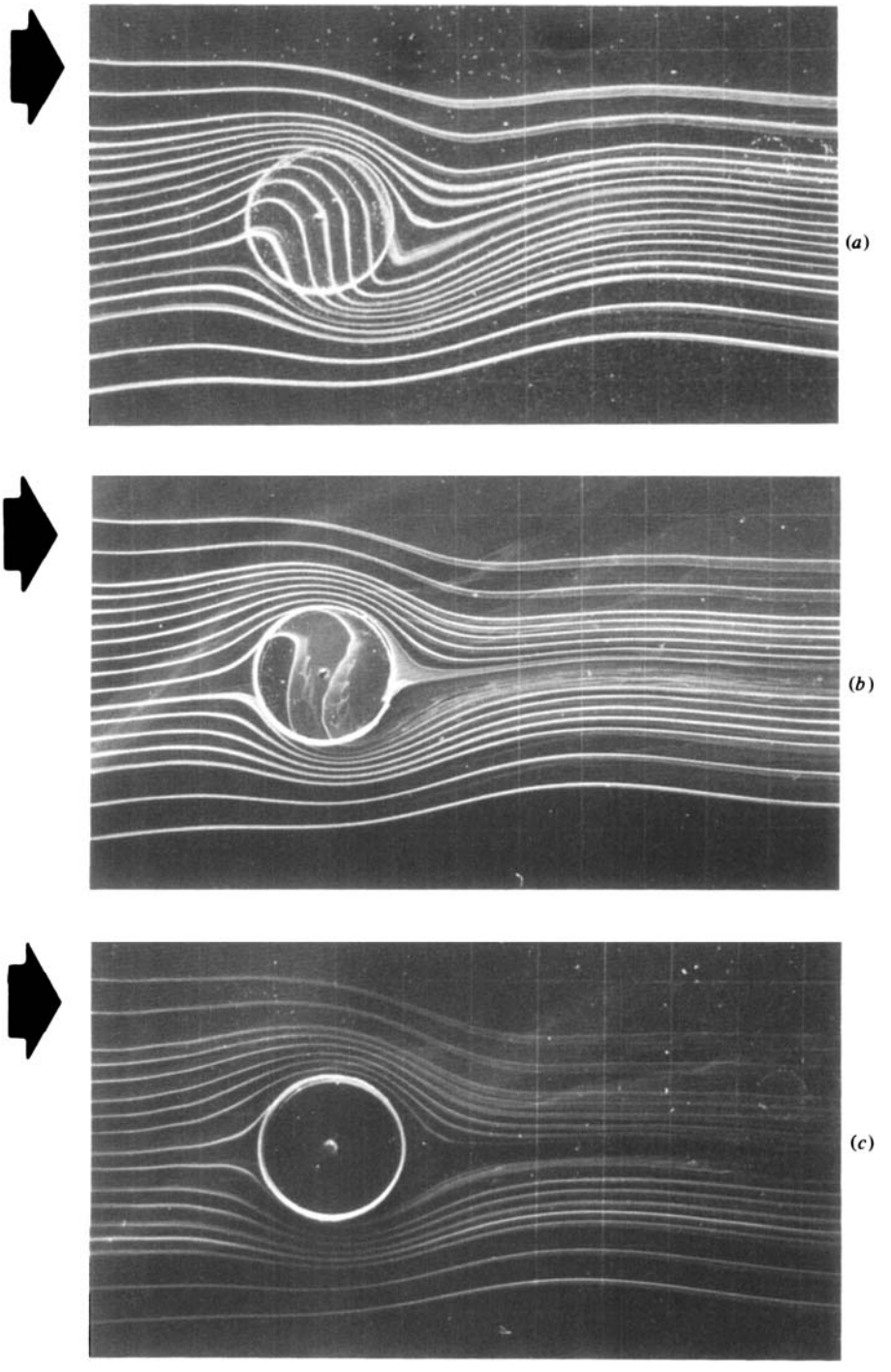

FIGURE 4. Midchannel streaklines; disk; $Ro = 9.8 \times 10^{-2}$, $E = 15.2 \times 10^{-4}$ ($Re = 64$), beta-plane eastward ($\beta = 0.40$), $R/H = 0.73$: (*a*) $2h/H = 0.25$; (*b*) $2h/H = 0.50$; (*c*) $2h/H = 0.75$.

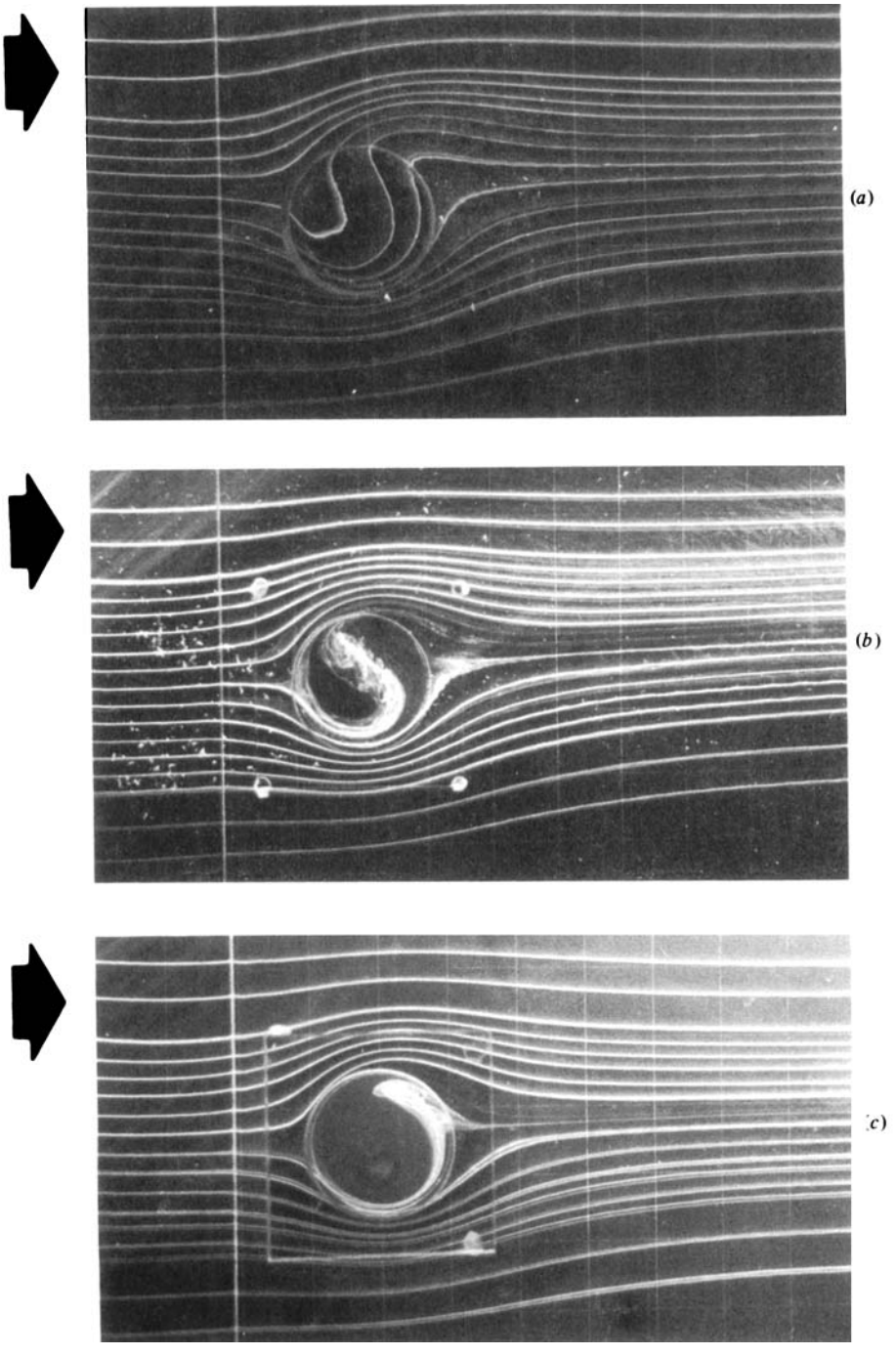

FIGURE 5. Midchannel streaklines; cylindrical depression; $Ro = 4.9 \times 10^{-2}$, $E = 7.2 \times 10^{-4}$ ($Re = 68$), f-plane ($\beta = 0.00$), $R/H = 0.73$: (*a*) $2h/H = 0.25$; (*b*) $2h/H = 0.75$; (*c*) $2h/H = 1.50$.

Taylor–Proudman theorem). The hazy tracer patterns to the right of the midplane streamlines above the disk in figure 4(*b*) are due to portions of the relatively dense tracer 'dropping' into Ekman boundary layers on the disk surface.

Figure 5 also shows the important effects of the depression aspect ratio, other system parameters being held fixed. These photographs are for an *f*-plane case with the flow being from left to right and the rotation anticlockwise. Note that the total depression depth (top and bottom) is 1.5 times the channel depth in figure 5(*c*). The amount of fluid passing over the depression decreases dramatically as the depression depth increases. It is noted that the 7.5×7.5 cm square enclosing the boundary of the circular depression in figures 5(*b*, *c*) (clearly visible in *c*) is the outline of Plexiglas extensions added above and below the flow channel to accommodate the large depressions for these two cases. The depression in figure 5(*a*) was made simply by drilling a 2.54 cm radius hole in the bounding walls of the channel.

Figure 6 depicts a series of runs for westward flow over a disk for increasing Rossby number (and decreasing β), other parameters being fixed. The flow is from right to left and the rotation is anticlockwise. It is noted that, as the Rossby number increases (and β decreases), the rate of flow through the imaginary cylinder circumscribing the disk increases. This is as expected sinces the constraints of the Taylor–Proudman theorem should become increasingly valid for smaller and smaller Rossby numbers.

It is also noted that with increasing Rossby number (and decreasing β) the flow in the vicinity of the disk has an increasing tendency to become unsteady. In figure 6(*b*), for example, the streaklines passing through the circumscribing cylinder and those adjacent to this cylinder indicate that a slight unsteadiness in the flow has developed; this flow in which the unsteadiness is restricted to a small region in the vicinity of the circumscribing cylinder and for which the amplitude of the wavelike patterns of the streaklines are much smaller than the obstacle diameter is termed 'slightly unsteady'. Flows in which the amplitude of the wave patterns are comparable to the obstacle diameter, such as that in figure 6(*c*), are termed 'fully unsteady'; in such flows the region of unsteadiness of the flow field extends well beyond (i.e. of the order of one or two diameters) the boundary of the circumscribing cylinder. It must be emphasized that the tracer lines in all of these photographs are streaklines and thus correspond to streamlines only for steady flow. When the flow is unsteady, as in figures 6(*b*, *c*), these lines are no longer streamlines. Thus, for example, the large wavelike patterns in the lower left-hand portion of figure 6(*c*) do not depict streamlines or particle pathlines. In fact, in the experiments considered, Ekman suction and pumping quickly dissipate unsteady motions in the vicinity of the circumscribing cylinder and within a few diameters downstream of the topography the motion is observed to be steady; i.e. the wavelike patterns are observed to be advected downstream with little change in shape.

The unsteady nature of the flow in the vicinity of the cylinder in figures 6(*b*, *c*) is similar. The unsteadiness is restricted to a region of less than a quarter of a diameter beyond the circumscribing cylinder in figure 6(*b*) and less than approximately one diameter in figure 6(*c*). In summary, for certain parameter ranges the flow in the immediate neighbourhood of the obstacle can become unsteady (probably through the development of a shear-layer instability as in the case of the solid cylinder in BD (1982) and when local unsteadiness occurs the streaklines shown on the laboratory figures can no longer be considered streamlines.

Figures 7(*a*, *b*) are Rossby number versus Ekman number flow-regime maps for the disk for the *f*-plane and beta-plane experiments respectively. The experimental photographs were characterized simply as steady (symbol only), slightly unsteady

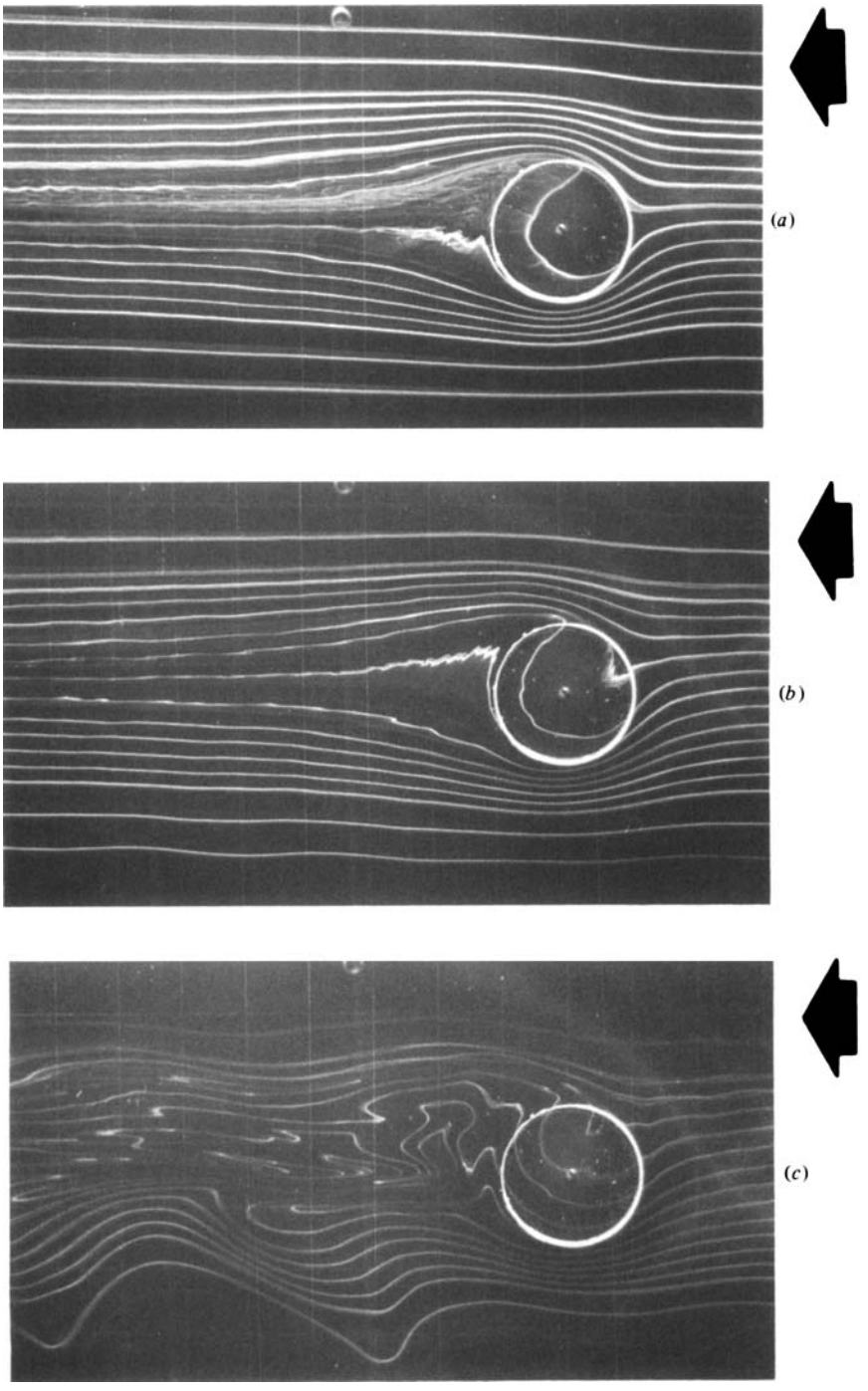

FIGURE 6. Midchannel streaklines; disk; $E = 7.4 \times 10^{-4}$, beta-plane westward, $2h/H = 0.50$, $R/H = 0.73$: (*a*) $Ro = 4.9 \times 10^{-2}$ ($Re = 66$), $\beta = 0.80$; (*b*) $Ro = 9.8 \times 10^{-2}$ ($Re = 133$), $\beta = 0.40$; (*c*) $Ro = 19.7 \times 10^{-2}$ ($Re = 266$), $\beta = 0.20$.

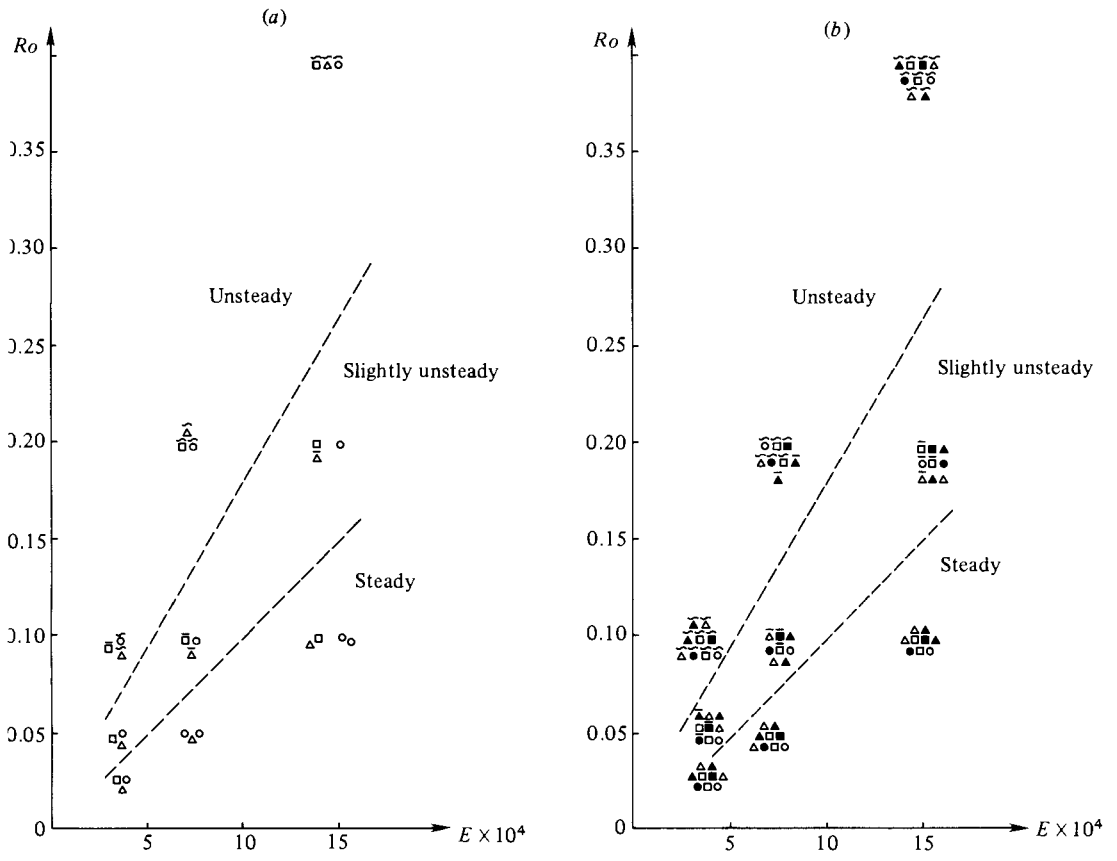

FIGURE 7. Rossby number versus Ekman number flow-regime maps for disk. Tilde (~) above symbol represents unsteady flow while overbar represents slightly unsteady flow (see text). Parameter values $R/H = 0.73$, $2h/H = 0.25$ (○), 0.50 (□) and 0.75 (△). (*a*) *f*-plane ($\beta = 0$); (*b*) beta-plane with open symbols being westward and closed symbols eastward. The dashed lines represent the approximate divisions between steady and slightly unsteady and slightly unsteady and steady flows respectively.

(overbar) or fully unsteady (tilde above symbol). Within the limitations of the experiment and for the range of parameters investigated it can be concluded that the unsteady nature of the flow depends primarily on the values of the Rossby and Ekman numbers and is essentially independent of the ratio $2h/H$ of disk height to channel depth, beta-parameter and flow direction.

Furthermore, similar plots for the cylindrical depression for the *f*-plane and beta-plane are virtually identical with figures 7(*a*, *b*) respectively, and for the sake of brevity are not included here. That is, the steady, slightly unsteady and fully unsteady flows occur in approximately the same regions of Rossby number versus Elman number space as for the disk; this also includes the experiments for the depression for values of $2h/H$ given by 1.50.

In order to quantify the experimental results, a 'Taylor-column speed' U_s is defined as the average speed of the fluid in the midchannel plane through the circle defined by the circumscribing cylinder and normalized on the freestream flow. Since the tracer spacing upstream of the topographic features was set at eight spaces for the disk diameter $2R = 5.08$ cm, one need merely count the number of spaces between

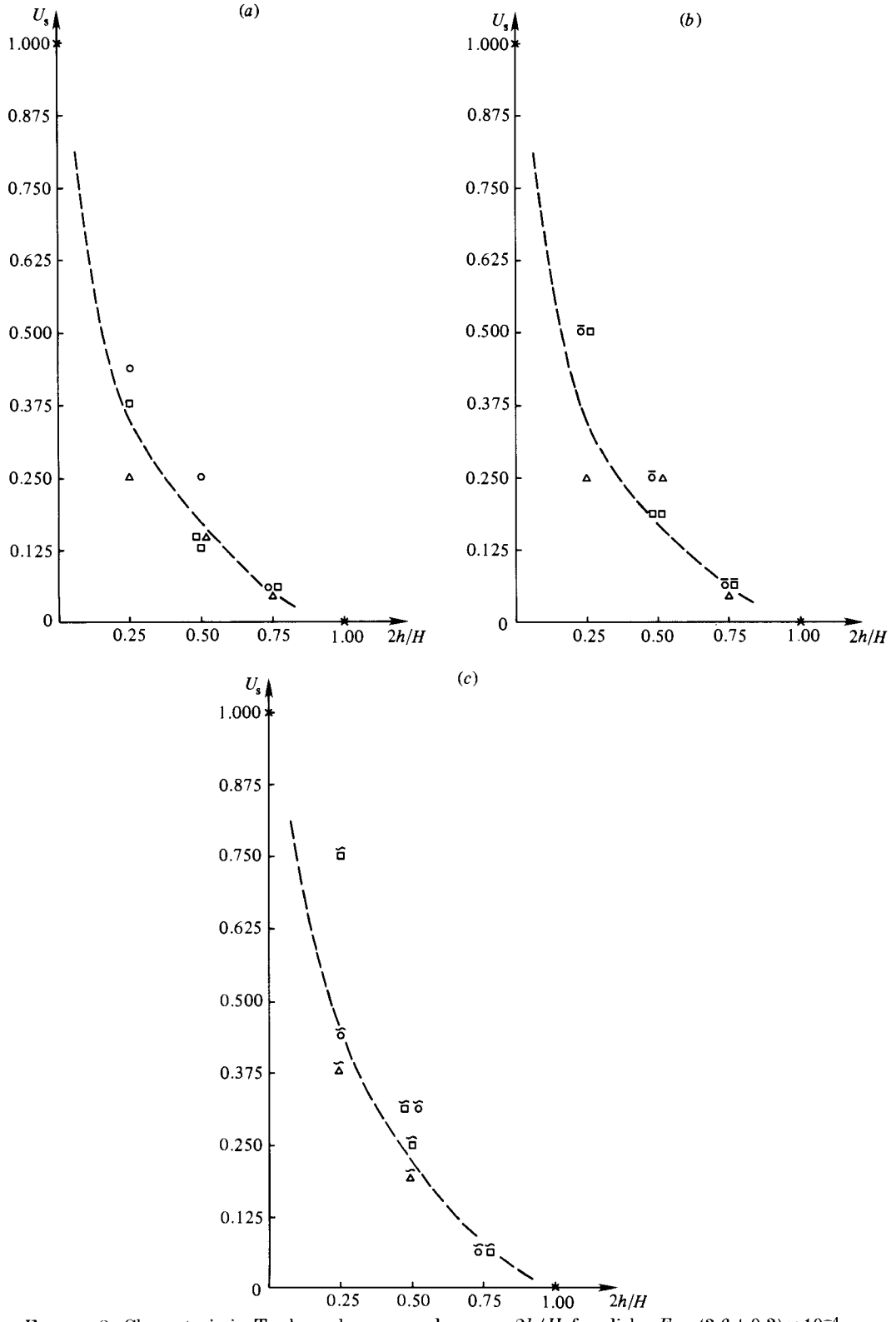

FIGURE 8. Characteristic Taylor-column speed versus $2h/H$ for disk; $E = (3.6 \pm 0.3) \times 10^{-4}$: △, f-plane; ○, eastward; □, westward. (*a*) $Ro = 2.5 \times 10^{-2}$ ($\beta = 1.60$); (*b*) $Ro = 4.9 \times 10^{-2}$ ($\beta = 0.80$); (*c*) $Ro = 9.8 \times 10^{-2}$ ($\beta = 0.40$).

streamlines crossing the circumscribing circle and divide by eight to obtain an estimate of the Taylor-column speed. While on many of the photographs it is possible to estimate a fraction of a spacing, the crowding of the streamlines along the circumscribing circle suggests the maximum error in this measurement to be approximately one spacing, or 12.5% for the Taylor-column speed. This observable, of course, has its shortcomings in that it does not address the question of flow direction or variation in speed across the circumscribing cylinder. Nevertheless, it is a relatively easily measured observable, it allows some comparison across experiments, and it serves as a satisfactory indicator of the flow behaviour.

Figures 8(*a–b*) depict the Taylor-column speed, U_s as a function of the ratio $2h/H$ of disk height to channel depth for increasing Rossby numbers and for approximately fixed Ekman numbers (the plus and minus range for the Ekman number is principally due to variations in the fluid viscosity caused by temperature variations). As in the previous notation, the overbar represents a slightly unsteady flow while the tilde denotes a fully unsteady motion.

As discussed earlier, the figures clearly show the strong dependence of U_s on $2h/H$. Furthermore, one can note from figure 8 that there is a tendency for U_s to increase as a result of increasing Ro (and decreasing β), other parameters being fixed. Within the accuracy of the measurement of U_s it is not possible to determine the importance of flow direction or β on the magnitude of U_s. That is, f-plane and beta-plane eastward and westward flows give approximately the same U_s, other parameters being equal. This is not the case for the cylindrical depression, as will be discussed below.

Figures 9(*a–c*) are another series of plots of U_s versus $2h/H$ for the disk, but at a larger Ekman number than for figure 8. Comparisons of figures 8(*b*) and 9(*a*) and figures 8(*c*) and 9(*b*) respectively reveal a tendency for larger U_s to occur for larger E, other parameters being fixed.

Figures 10 and 11 are experimental runs for the cylindrical depression corresponding respectively to the parameters in figures 8 and 9 for the disk. From all of these figures one can again note the important dependence of U_s on the parameter $2h/H$; i.e. deeper depressions give smaller U_s. For the case of the disk, of course, U_s by definition is zero for $2h/H = 1$ (the cylinders fill the whole channel). This is not true for the depression, but one can note the continual decrease in U_s as $2h/H$ becomes larger.

The most apparent difference between figures 8 and 9 and figures 10 and 11 respectively is that for the disk it was not possible to determine an effect of flow direction on U_s, but for the depression it is clear that U_s is greater for westward flow than for f-plane or eastward flow, other parameters being fixed. As depicted on figures 10 and 11, within the limitations of the observations, it is not possible to distinguish between f-plane and eastward flow in the behaviour of U_s. As noted, however, the westward and f-plane and eastward flows differ substantially as regards U_s especially for the lower-Rossby-number flows.

As might be expected by comparing figures 8(*a*) and 10(*a*), figures 8(*b*) and 10(*b*), and so on, one can conclude that disks give stronger Taylor columns (i.e. smaller U_s) than cylindrical depressions for all values of $2h/H$, other parameters being fixed. Finally, in the case of the cylindrical depression the tendency for decreasing Ro (increasing β) or decreasing E to result in decreasing U_s, other parameters being fixed, can also be noted by considering figures 10 and 11.

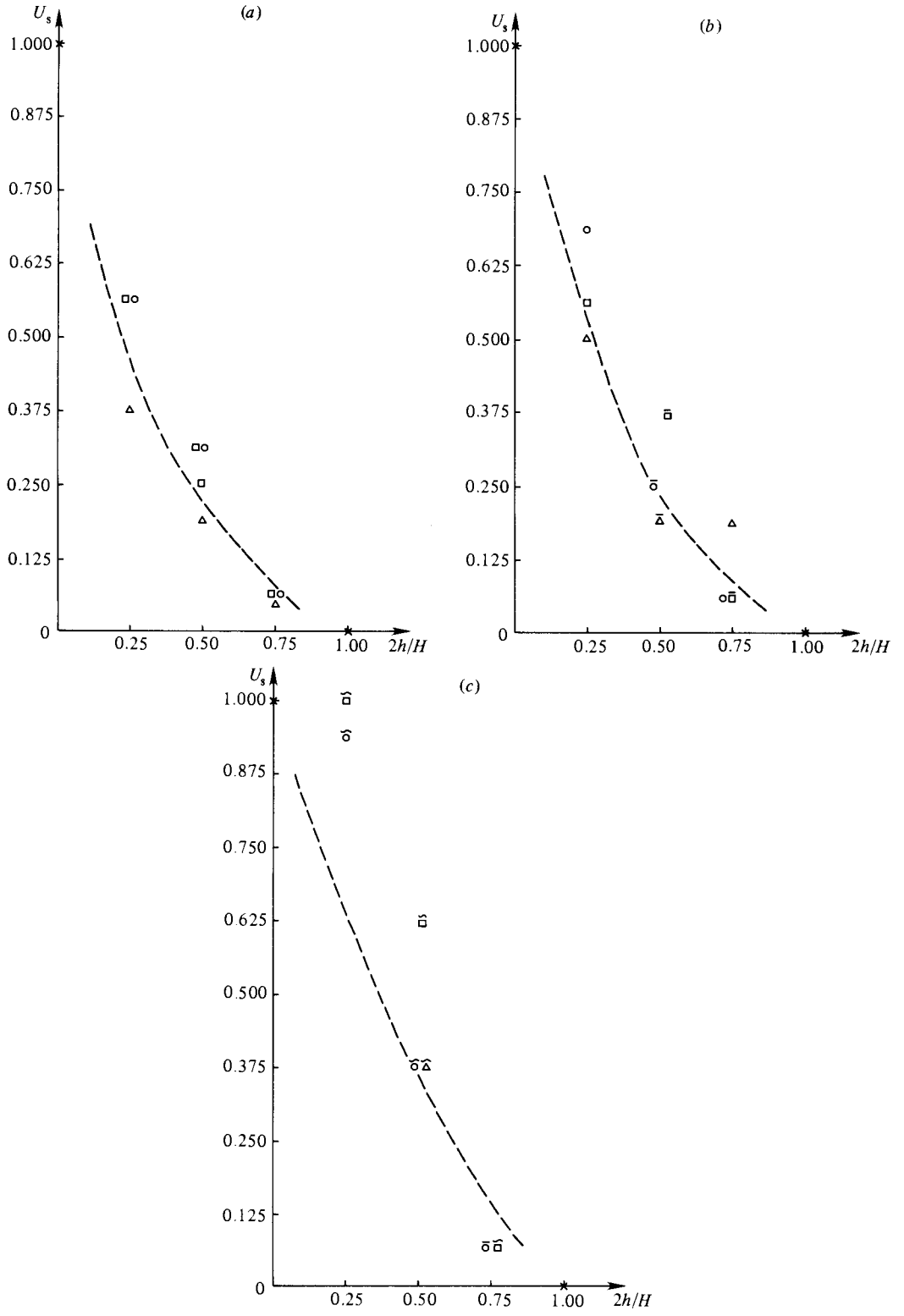

FIGURE 9. Characteristic Taylor-column speed versus $2h/H$ for disk: $E = 7.3 \pm 0.4 \times 10^{-4}$: △, f-plane; ○, eastward; □, westward. (*a*) $Ro = 4.9 \times 10^{-2}$ ($\beta = 0.80$); (*b*) $Ro = 9.8 \times 10^{-2}$ ($\beta = 0.40$); (*c*) $Ro = 19.7 \times 10^{-2}$ ($\beta = 0.20$).

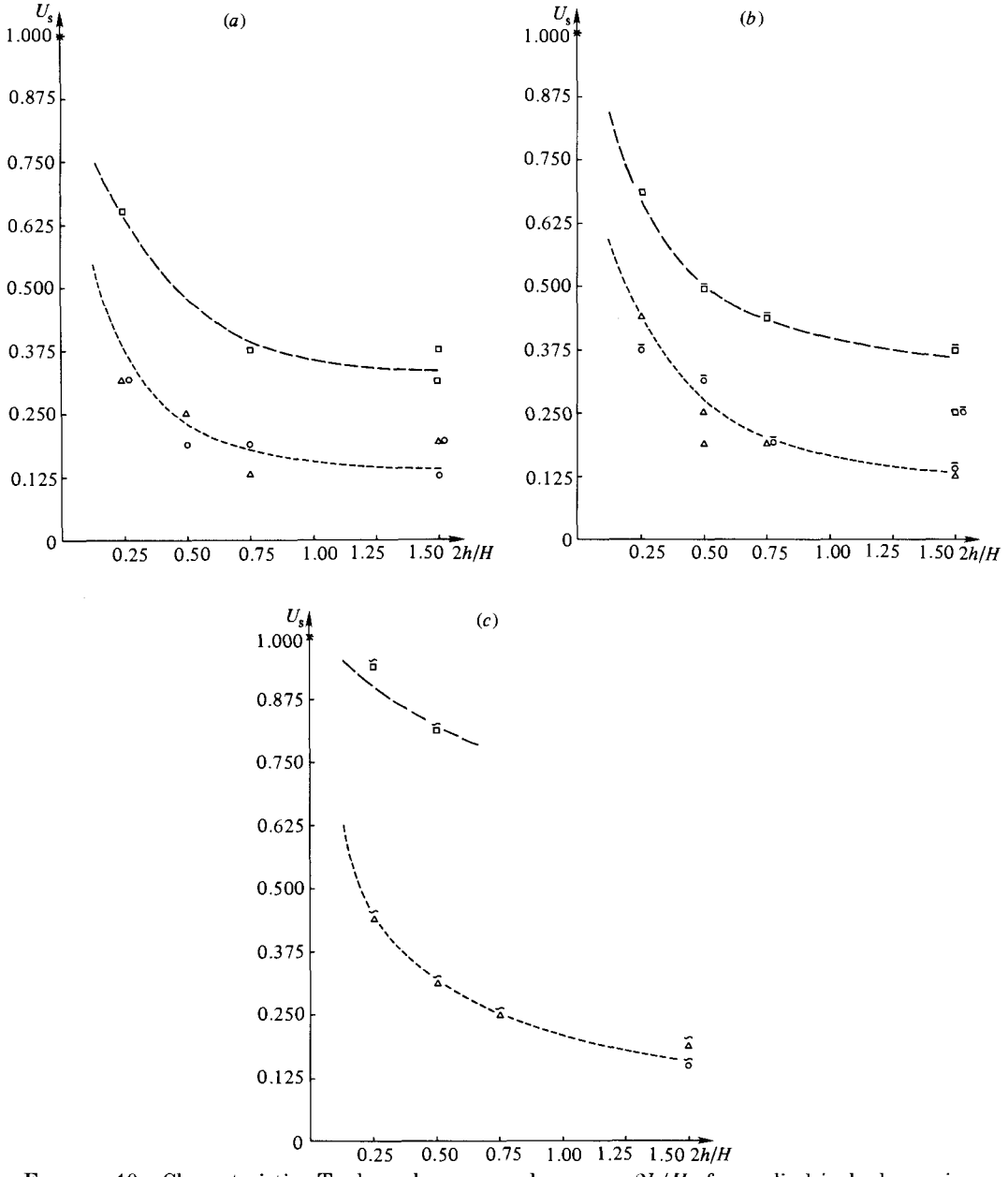

FIGURE 10. Characteristic Taylor-column speed versus $2h/H$ for cylindrical depression; $E = (3.4 \pm 0.3) \times 10^{-4}$: △, f-plane; ○, eastward; □, westward. (*a*) $Ro = 2.5 \times 10^{-2}$ ($\beta = 1.60$); (*b*) $Ro = 4.9 \times 10^{-2}$ ($\beta = 0.80$); (*c*) $Ro = 9.8 \times 10^{-2}$ ($\beta = 0.40$).

3. The quasigeostrophic potential-vorticity equation with friction and topography

The quasigeostrophic vorticity equation, including Ekman as well as lateral friction in a region of variable depth, is well known to meteorologists and oceanographers (Pedlosky 1979, particularly chap. 4). In this case, the local vorticity balance depends upon several competing tendencies: the advection of vorticity,

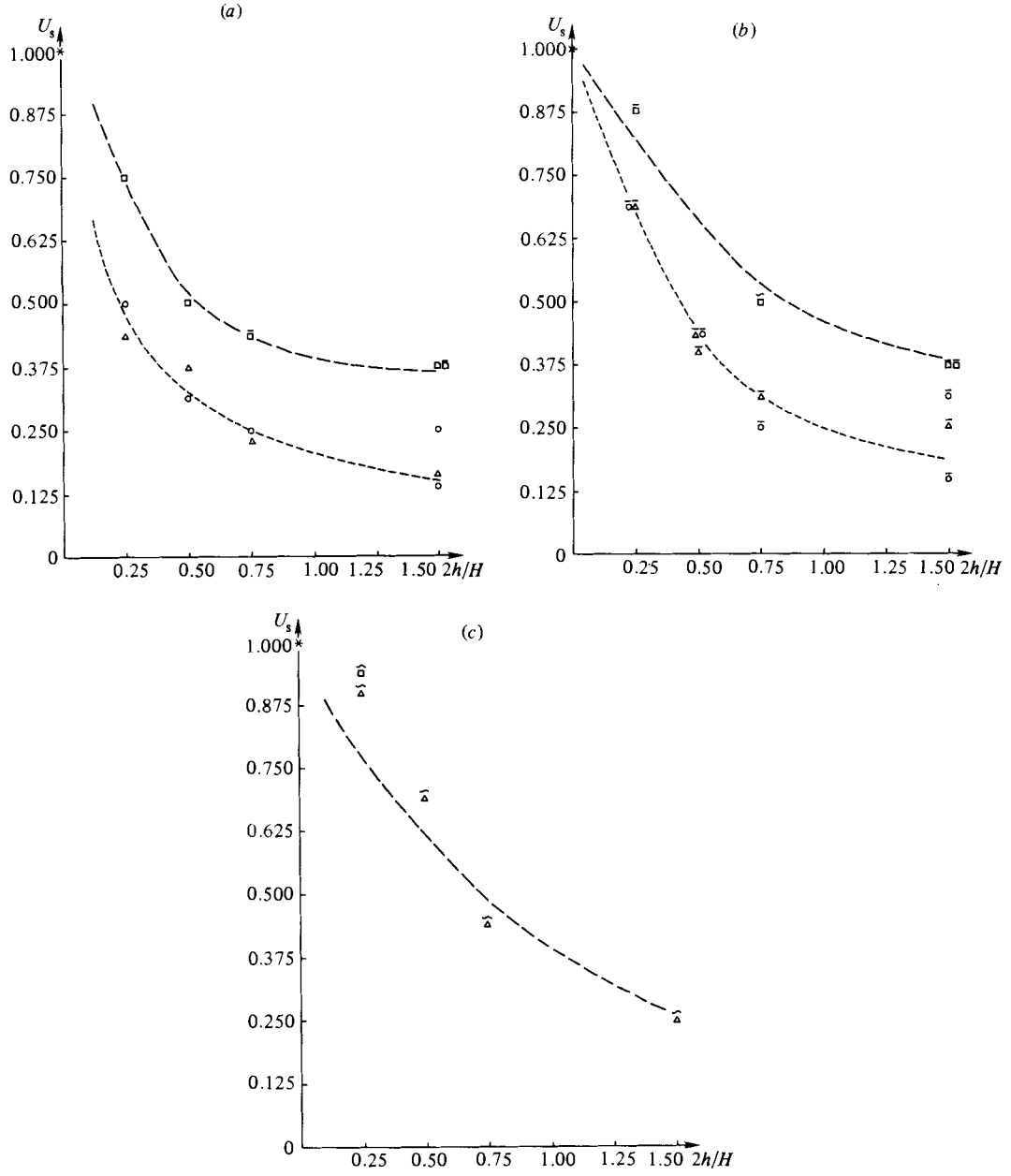

FIGURE 11. Characteristic Taylor-column speed versus $2h/H$ for cylindrical depression; $E = (6.9 \pm 0.4) \times 10^{-4}$: f-plane; ○, eastward; □, westward. (*a*) $Ro = 4.9 \times 10^{-2}$ ($\beta = 0.80$); (*b*) $Ro = 9.8 \times 10^{-2}$ ($\beta = 0.40$); (*c*) $Ro = 19.7 \times 10^{-2}$ ($\beta = 0.20$).

vortex-tube stretching (due both to variable depth and to Ekman-layer pumping on the upper and lower boundary surfaces) and frictional decay. Thus, following Pedlosky, the lowest-order z-component of the vorticity equation, in dimensional form, can be written as

$$\frac{D\xi_0}{Dt} = 2\omega \frac{\partial w_1}{\partial z} + \nu \nabla^2 \xi_0, \tag{3.1}$$

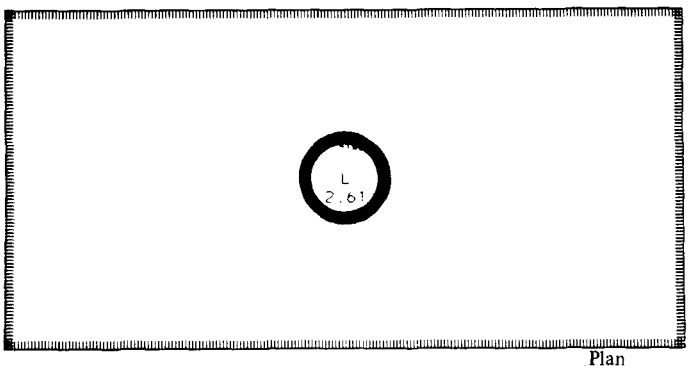

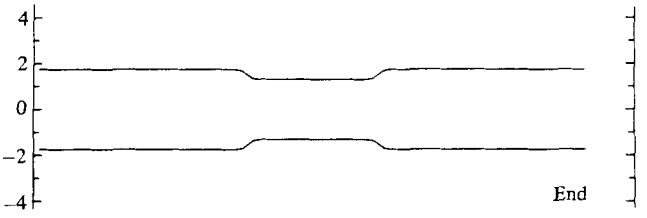

(*a*)

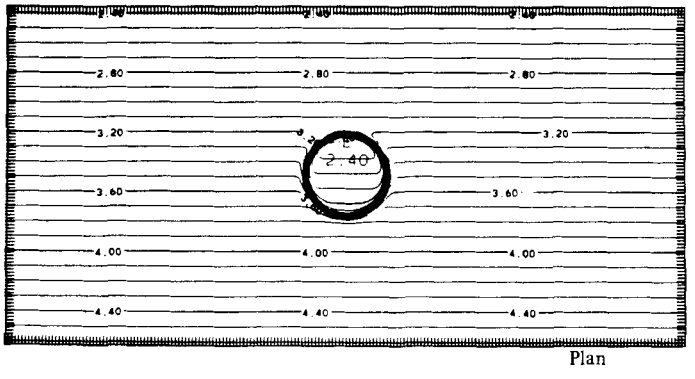

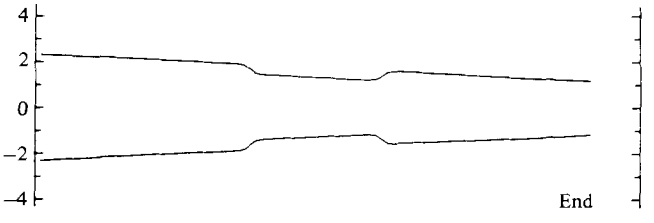

(*b*)

FIGURE 12. Schematic representation of topography used in the numerical experiments showing plan and end views (note the scale distortion). (*a*) $\alpha = 0$ or f-plane case; $h = 0.44$ cm, $H = 3.49$ cm, $R = 2.54$ cm, $L = 35.6$ cm and $W_0 = 0.10$ cm. (*b*) Beta-plane in which $\alpha = 0.0536$ with the other parameters as in (*a*). Note that the numerical values of the contours are in cm.

where ξ_0 is the vorticity of the geostrophic flow and w_1 is the vertical velocity in the interior. For our channel geometry (essentially figure 1 but with the sidewalls of the obstacle not vertical)

$$\frac{\partial w_1}{\partial z} = \bar{v}_0 \cdot \nabla \eta - \left(\frac{\nu}{\omega H^2}\right)^{\frac{1}{2}} \xi_0, \tag{3.2}$$

where $\bar{v}_0 = (u_0, v_0)$ is the horizontal velocity and

$$\eta = \frac{2\delta(x,y)}{H} - \frac{2y \tan \alpha}{H} \tag{3.3}$$

is the relative thickness of the fluid layer. Here $\delta(x,y)$ describes the shape of the isolated obstacle and $y \tan \alpha$ simulates the beta-effect. The factor 2 arises because both top and bottom boundaries have the same depth variations as in figure 1. Introducing the stream function, we can then write the quasigeostrophic potential vorticity equation as

$$\frac{\partial Q}{\partial t} + \mathrm{J}(\psi, Q) = -2\left(\frac{\omega\nu}{H^2}\right)^{\frac{1}{2}} \nabla^2\psi + \nu\nabla^4\psi, \tag{3.4}$$

Here

$$Q = \nabla^2\psi - \frac{4\omega}{H}\delta + \frac{4\omega \tan \alpha}{H} y \tag{3.5}$$

is the potential vorticity, a quantity that would be conserved along streamlines in the absence of the frictional terms on the right-hand side of (3.4).

Equation (3.4) will be used to simulate the laboratory flows discussed above. The circular disk or depression used there will be approximated (see §2) by a circular topographic feature of the form

$$\delta = h\left(\tfrac{1}{2} - \tfrac{1}{2}\tanh\frac{r-R}{W_0}\right), \tag{3.6}$$

where $r^2 = x^2 + y^2$; here h and R denote the height and radius respectively of the topographic feature, and W_0 is the characteristic width of the sidewalls. Note that δ goes from zero to h as it crosses the sidewalls. Figure 12 shows the shape of this topography in vertical section and planform. In all the experiments to be performed, W_0 is small compared with R; that is, we are dealing with a steep sidewall slope.

4. Numerical techniques

The numerical calculations are carried out by integrating (3.4) forward in time from a state of uniform undisturbed flow (either eastward or westward). Standard second-order-accurate finite-difference equations are used for the horizontal spatial derivatives with the Arakawa (1966) form for the advective (Jacobian) terms. This finite-differencing is used extensively in ocean and atmospheric models to conserve numerically the important flow properties (Holland 1978).

The equations are integrated in time using centred time differencing except for an occasional forward time step to eliminate time splitting of the solutions. The frictional terms are lagged one time step for stability reasons. The method of solution is to predict $\nabla^2\psi$ at a new time level using (3.4), to solve $\nabla^2\psi = F$ in a channel geometry with $\psi(y)$ specified at inflow (uniform $U = -\psi_y$), $\psi_x = 0$ specified at the outflow, $\psi = \frac{1}{2}UL$ on $y = -\frac{1}{2}L$, and $\psi = -\frac{1}{2}UL$ on $y = +\frac{1}{2}L$, and making use of a fast-Fourier-transform technique for the solution of the Poisson equation.

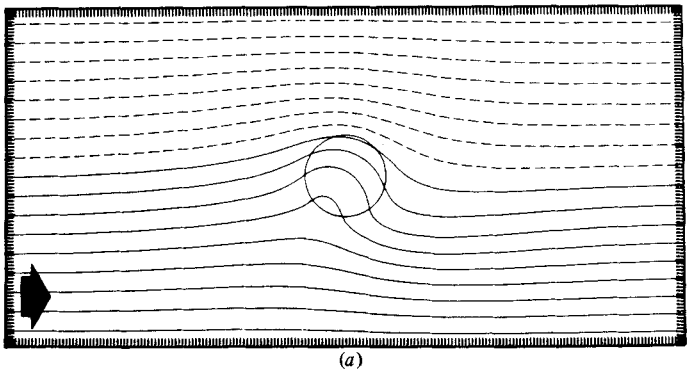

(a)

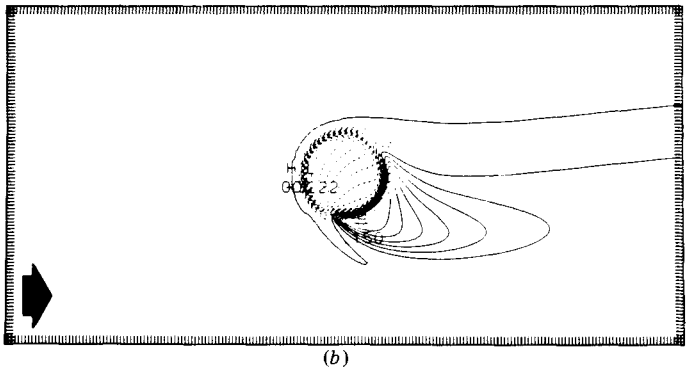

(b)

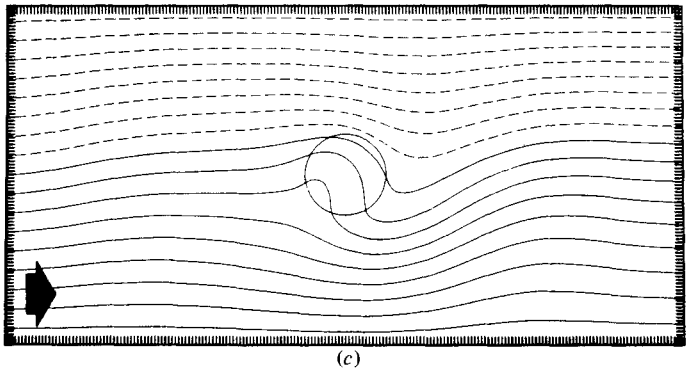

(c)

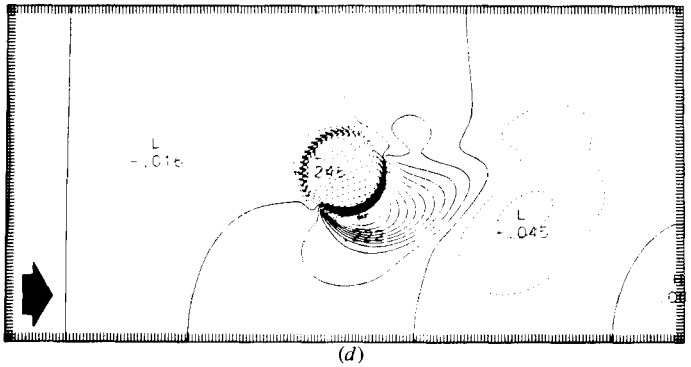

(d)

FIGURE 13(a–d). For caption see facing page.

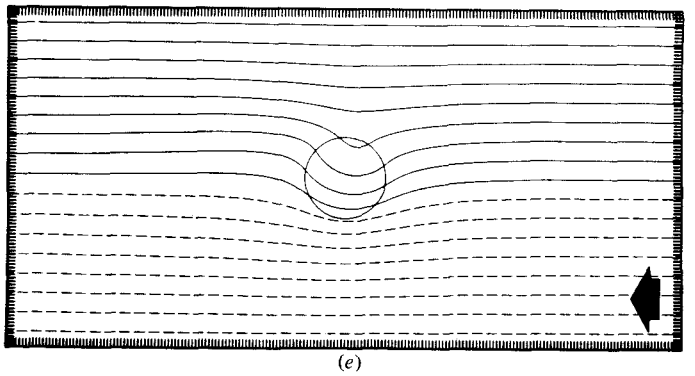

(*e*)

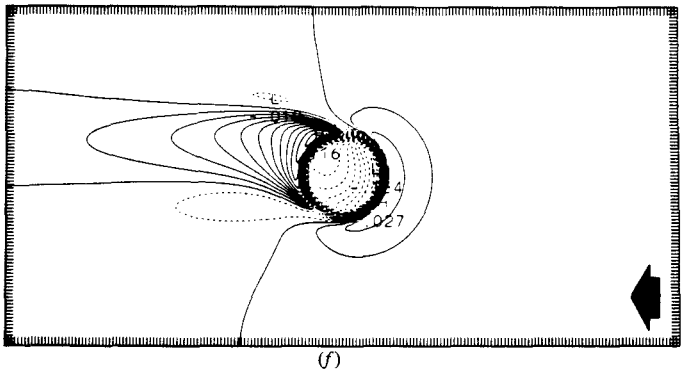

(*f*)

FIGURE 13. Numerical experiments for a disk simulating the respective laboratory experiments in figure 2. Dimensional parameters all figures: $R = 2.54$ cm, $H = 3.49$ cm, $L = 21.2$ cm, $h = 0.44$ cm, $\omega = 0.5$ rad/s, $U = 0.25$ cm/s. Dimensionless parameters, all figures: $Ro = 9.8 \times 10^{-2}$, $E = 15.4 \times 10^{-4}$ ($Re = 64$), $2h/H = 0.25$, $R/H = 0.73$. (*a*, *b*) f-plane, $\alpha = 0$, $\beta = 0$; (*c*, *d*) beta-plane eastward, $\alpha = 0.0536$, $\beta = 0.40$; (*e*, *f*) beta-plane westward, $\alpha = 0.0536$, $\beta = 0.40$. (*a*, *c*, *e*) are streamlines ψ, and (*b*, *d*, *f*) are constant-vorticity $\nabla^2\psi$ contours. The respective contour intervals are (*a*) 0.3 cm^2 s^{-1}, (*b*) 0.02 s^{-1}, (*c*) 0.3 cm^2 s^{-1}, (*d*) 0.02 s^{-1}, (*e*) 0.3 cm^2 s^{-1}, (*f*) 0.01 s^{-1}. Dashed isolines indicate negative values for both fields. The H and L and their associated numbers designate local maxima and minima respectively.

In addition to specifying ψ on inflow and $\psi_x = 0$ on outflow, further boundary conditions on vorticity are needed because of the lateral friction terms. The outflow boundary gives little difficulty; the auxiliary boundary condition $\nabla^2\psi_x = 0$ leads to smooth outflow behaviour. Eastward β-plane flow cases, however, are sensitive to the auxiliary *inflow* condition, apparently due to westward-propagating Rossby waves reaching the upstream end during the spinup to a steady state. Several upsteam boundary conditions have been tried, including (i) specifying $\nabla^2\psi = 0$ and (ii) specifying $V = \psi_x = 0$ on inflow. The former choice leads, for our standard domain size, to a permanent disturbance (a non-zero V-component at the inflow boundary). Alternatively, when ψ_x is set to zero, no disturbance remains in the final steady state. In fact, $\nabla^2\psi$ is nearly zero at the inflow, suggesting that this boundary condition more effectively lets the westward-propagating waves exit from the domain. All cases shown below used this condition. It should be mentioned, however, that the nature of the flow near the disk was little affected by any of these 'distant' boundary conditions, as long as the inflow boundary was several radii away from the obstacle.

A few experiments with different domain sizes were carried out to ascertain how

the flow depended upon this factor. In addition, numerical experiments with varying grid resolution were carried out to assess the importance of numerical errors due to the finite-difference approximations involved. These auxiliary experiments will be discussed after presenting basic simulations of the laboratory experiments. For these the disk or depression has a diameter of 2.54 cm located at the centre of a channel 42.4 cm long and 21.2 cm wide. The grid size is 0.212 cm so that numerical solutions are obtained on a 200×100 grid of points. As we shall show later, this is adequate to describe in detail the flow over and in the vicinity of the obstacle.

5. Numerical experiments

The initial numerical experiments were carried out to simulate the laboratory flow fields shown in figure 2. Results are shown in figure 13. Note firstly that the deflections of the streamlines are rather well reproduced, showing the correct tendencies for (i) southward deflections (figure 13*a*, *c*), (ii) Rossby-lee-wave structure for eastward flow on the beta-plane (figute 13*c*) as well as the absence of any such structure for westward flow on the beta-plane (figure 13*e*), and (iii) the magnitude of the flow velocity over the obstacle (all cases).†

The disturbance patterns, as indicated by the simulated vorticity patterns, are shown in figures 13(*b*, *d*, *f*). The influence of β is clearly shown: a stationary Rossby lee wave exists when the westward-propagating tendency is arrested by 'mean' eastward flow (figure 13*d*). A rapidly decaying downstream oscillation occurs. Owing to the top and bottom Ekman layers, however, the vorticity in all cases is largest over the obstacle and immediately on its lee side, and decays rapidly away downstream. For these parameters, the obstacle disturbs the flow only within a few radii of the topographic feature.

The streamline and vorticity patterns shown in figures 13(*a*, *b*) are easily explained by following a streamline across the topographic feature and examining the changing vorticity along its path. The case with $\alpha = 0$ (i.e. no beta-effect) is particularly simple to interpret. Upstream, the vorticity $\xi_0 = \nabla^2\psi$ is virtually zero, but, as the flow crosses the leading edge of the topography, there is a rapid decrease in vorticity equivalent to $4\omega h/H$. The changing vorticity is predictable from (3.4) by assuming that the potential vorticity Q is approximately conserved crossing the topographic slope, since then $|\nabla\xi_0| = 4\omega\,\Delta\delta/H = 4\omega h/H$. The minimum value of ξ_0 is correctly predicted to about 10% using this total stretching input of negative vorticity. This vorticity manifests itself as a clockwise curvature of the flow over the flat top of the obstacle. For the parameters of this case, the Ekman-pumping terms lead to a decrease of (negative) vorticity quite rapidly along a streamline from this nearly impulsive topographic input. In the flat region on top of the disk

$$\bar{v}_0 \cdot \nabla\xi_0 \approx -2\left(\frac{\omega\nu}{H^2}\right)^{\frac{1}{2}}\xi_0, \tag{5.1}$$

i.e. the vorticity decays by Ekman suction. This gives an estimate for the frictional e-folding scale

$$L_\delta \approx \frac{U}{2(\omega\nu/H^2)^{\frac{1}{2}}}, \tag{5.2}$$

which is about 6.2 cm for the parameters given in figure 13(*a*, *b*). Thus the vorticity will have decreased by a factor of about e^{-1} before the streamline reaches the other

† Note that the spacing of the streaklines in the laboratory is non-uniform (i.e. the outer spacing is twice the inner), while that in the numerical simulations is uniform.

edge of the disk (note that the diameter of the disk is 5.08 cm). When the streamline crosses into deeper water again there is another impulsive change in vorticity (this time positive), which leads to counterclockwise curving streamlines. These merge smoothly back onto the uniform flow far from the obstacle.

The role of the beta-effect in these experiments (laboratory and numerical) can be appreciated by examining the size of the terms in the linearized vorticity balance:

$$U\psi_{xxx}+\frac{4\omega\tan\alpha}{H}\psi_x=-\left(\frac{4\omega\nu}{H^2}\right)^{\frac{1}{2}}\psi_{xx}. \tag{5.3}$$

Letting $\psi\sim e^{mx}$, then

$$Um^2+\left(\frac{4\omega\nu}{H^2}\right)^{\frac{1}{2}}m+\frac{4\omega\tan\alpha}{H}=0 \tag{5.4}$$

gives the characteristic equation governing the nature of the downstream decay for this simplified problem. When $\tan\alpha=0$ there is a single decay scale given by (5.2) above. When $\tan\alpha\neq 0$ and $U>0$, and when, as in all of the laboratory experiments, $\tan\alpha>\nu/4HU$ the m_i are complex with a single exponential downstream decay scale twice that above (12.4 cm) and an oscillation wavelength given by

$$L_0=\frac{2\pi}{k}=\frac{2\pi}{\left(\frac{4\omega\tan\alpha}{UH}-\frac{\omega\nu}{U^2H^2}\right)^{\frac{1}{2}}}. \tag{5.5}$$

For the laboratory experiments shown in figures 2(*b*), 3(*b*), 4(*a–c*) and for the numerical experiments given in figures (13(*c*), 14(*a*, *c*, *e*), L_0 has the value of 18.4 cm. Finally, when $\tan\alpha\neq 0$ and $U<0$ the m_i are again real with two distinct decay scales, one upstream and one downstream (differing signs):

$$L_{\rm up}^{-1}=m_{\rm d}=\left(\frac{\omega\nu}{H^2U^2}\right)^{\frac{1}{2}}-\left(\frac{\omega\nu}{H^2U^2}+\frac{4\omega\tan\alpha}{H|U|}\right)^{\frac{1}{2}}, \tag{5.6}$$

$$L_{\rm dn}^{-1}=m_{\rm d}=\left(\frac{\omega\nu}{H^2U^2}\right)^{\frac{1}{2}}+\left(\frac{\omega\nu}{H^2U^2}+\frac{4\omega\tan\alpha}{H|U|}\right)^{\frac{1}{2}}. \tag{5.7}$$

For the laboratory experiment shown in figure 2(*c*) and the numerical experiment given in figure 13(*f*), one determines $L_{\rm up}=3.6$ cm and $L_{\rm dn}=2.3$ cm. These scales agree reasonably well with estimates made from the vorticity pictures in figure 13(*f*). Qualitatively, the beta-eastward experiment differs from the $\beta=0$ experiment by reaching further downstream and by showing an oscillation in the wake of the obstacle. The beta-westward case differs from the others by having two decaying roots, one upstream and one downstream, and we see in figure 13(*f*) that there is indeed a disturbance upstream of the obstacle (as well as downstream) which is not the case for the other two numerical experiments.

In order to test other parts of the parameter range, numerical analogues of the laboratory experiments shown in figures 3–6 were also run. Here only the cases equivalent to those in figures 4 and 6 are shown; these are given in figures 14 and 15 respectively. The behaviour of the flow for the sequence of taller and taller obstacles shown for the laboratory cases (figures 4*a–c*) is similar to the numerical simulations (figures 14*a*, *c*, *e*). When the height of the topographic feature is doubled (comparison of figures 14*a* and *c*), the amount of flow going over the obstacle is greatly reduced, and when the height h is tripled (comparison of figures 14*a* and *e*), almost all of the flow diverts around the obstacle. At this extreme a Taylor-column situation has approximately been reached, and the fluid over the obstacle is nearly isolated.

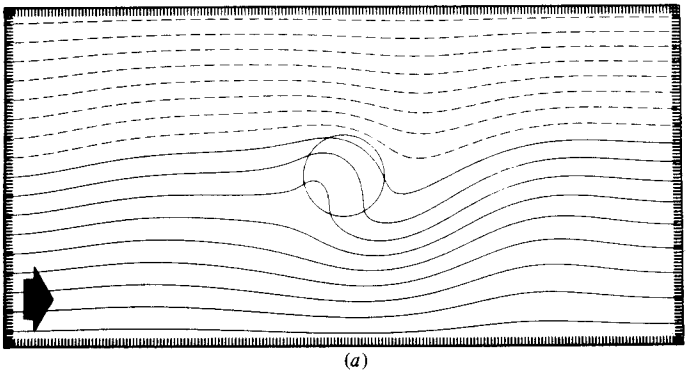

(a)

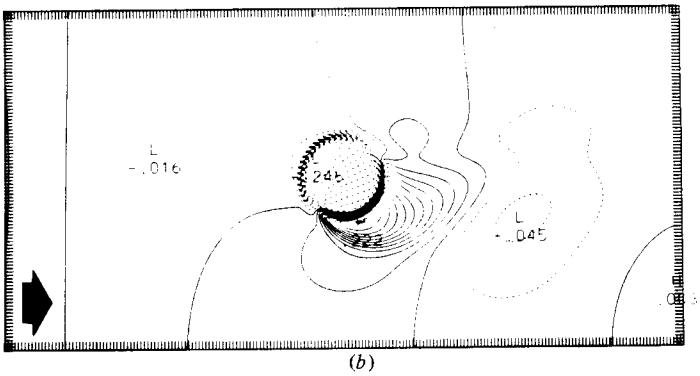

(b)

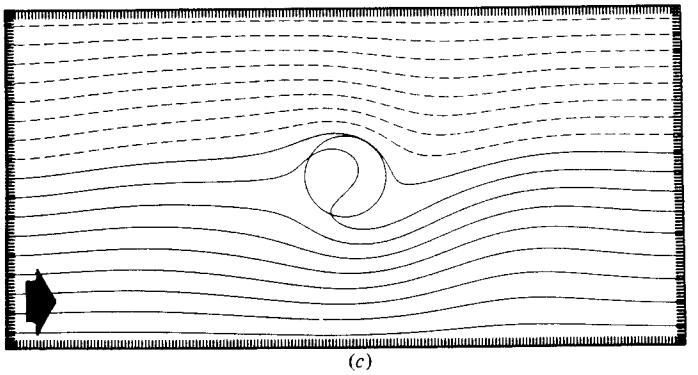

(c)

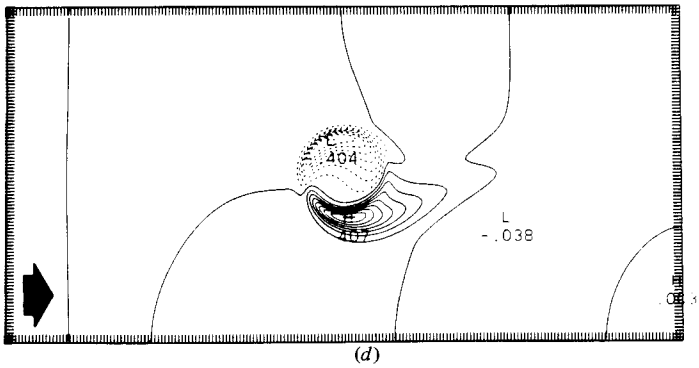

(d)

FIGURE 14(a–d). For caption see facing page.

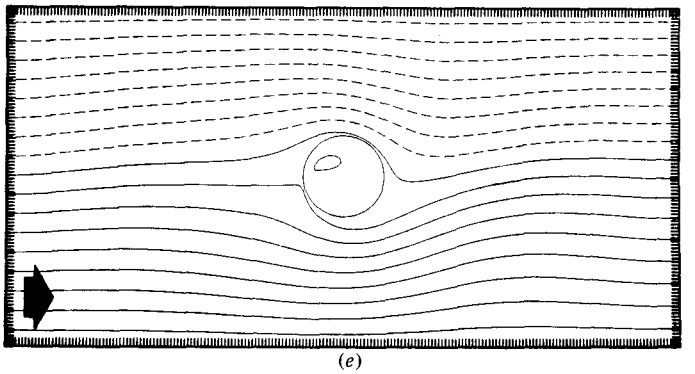

(*e*)

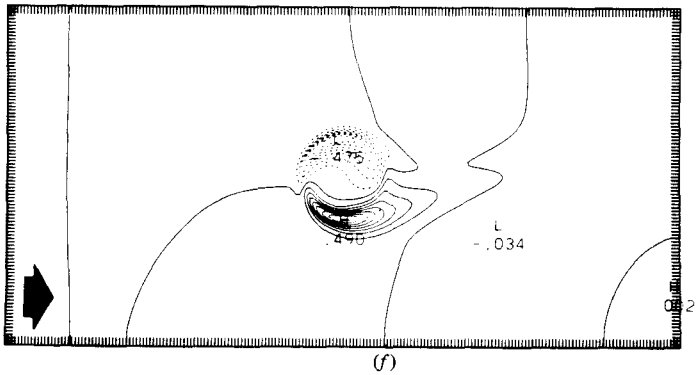

(*f*)

FIGURE 14. Numerical experiments for a disk in eastward flow simulating the respective laboratory experiments in figure 4. Dimensional parameters, all figures: $R = 2.54$ cm, $H = 3.49$ cm, $L = 21.2$ cm, $\omega = 0.5$ rad/s, $U = 0.25$ cm/s, and $\alpha = 0.0536$. Dimensionless parameters, all figures: $Ro = 9.8 \times 10^{-2}$, $E = 15.4 \times 10^{-4}$ ($Re = 64$), $\beta = 0.40$, $R/H = 0.73$. (*a*, *b*) $h = 0.44$ cm, $2h/H = 0.25$; (*c*, *d*) $h = 0.88$ cm, $2h/H = 0.50$; (*e*, *f*) $h = 1.32$ cm, $2h/H = 0.75$. The respective contour intervals are (*a*) 0.3 cm^2 s^{-1}, (*b*) 0.02 s^{-1}, (*c*) 0.3 cm^2 s^{-1}, (*d*) 0.05 s^{-1}, (*e*) 0.3 cm^2 s^{-1}, (*f*) 0.06 s^{-1}.

These numerical results are in good agreement with the laboratory observations of figures 4(*a–c*).

In the sequence shown in figures 15(*a*, *c*, *e*) (comparable with laboratory flows in figures 6*a–c*) a difference between the numerical simulations and the laboratory analogues is observed. The principal difference is the absence of transient behaviour in the numerical calculations. For the Reynolds numbers under consideration ($Re = 270$ in figure 15*e*) it would not be surprising for instabilities to begin to manifest themselves. This is not observed in the numerical experiments, perhaps owing to the idealized nature of the numerical model (i.e. exact steadiness in the upstream flow and complete two-dimensionality). These conditions may not be entirely met in the laboratory situation.

As a test, the sequence shown in figures 15(*a–c*) was extended to very strong flows ($Re = 1064$), as shown in figure 16, and there was still no apparent transient behaviour observed. This case was of some interest, however, in that for the first time (not so for other experiments discussed here), the flow was so strong that friction did not play a very important role. There was a strong tendency along all streamlines for the potential vorticity to be conserved. In the vorticity balance the change in relative vorticity following a streamline almost exactly compensates for the

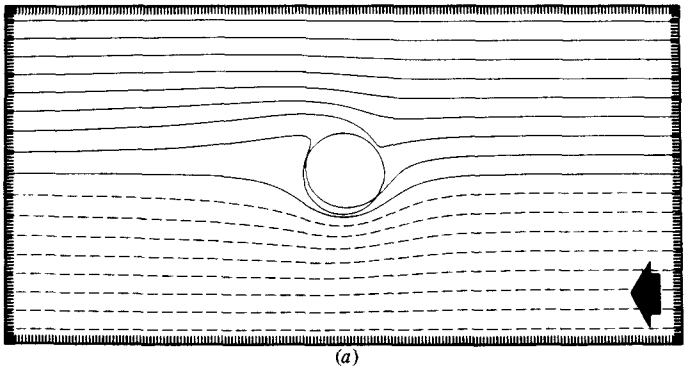

(a)

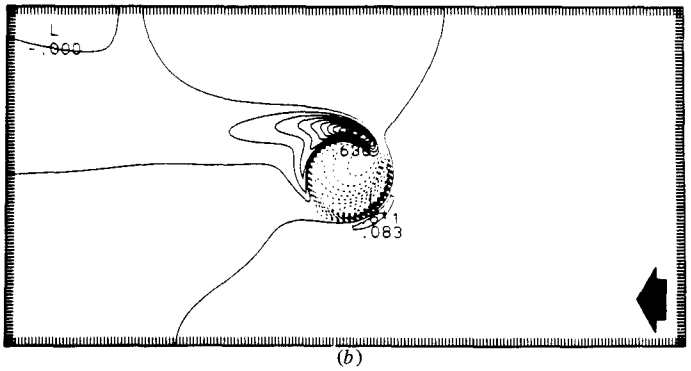

(b)

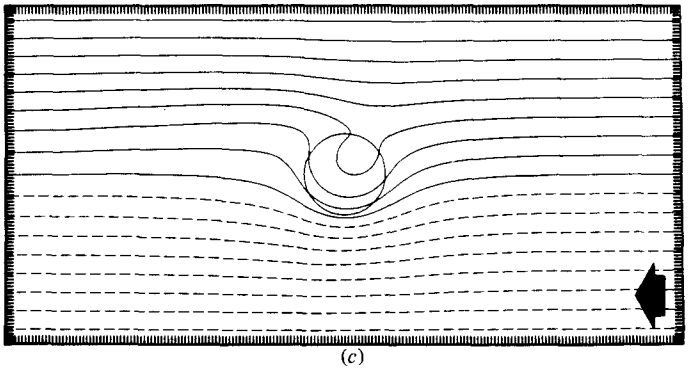

(c)

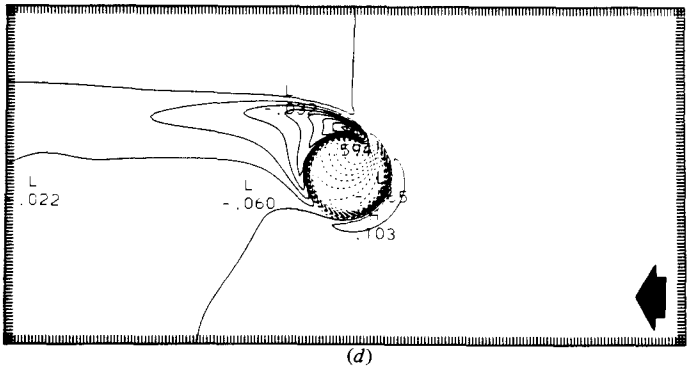

(d)

FIGURE 15(a–d). For caption see facing page.

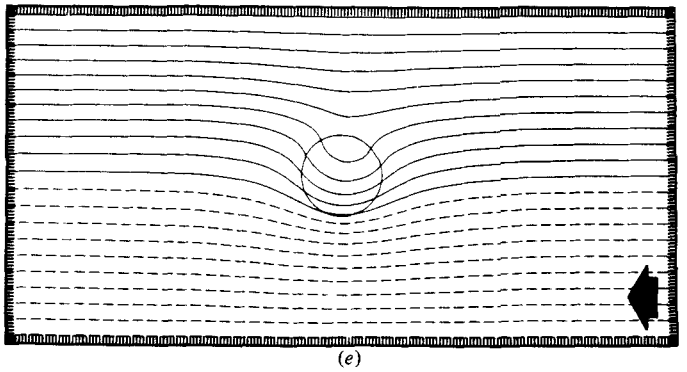

(*e*)

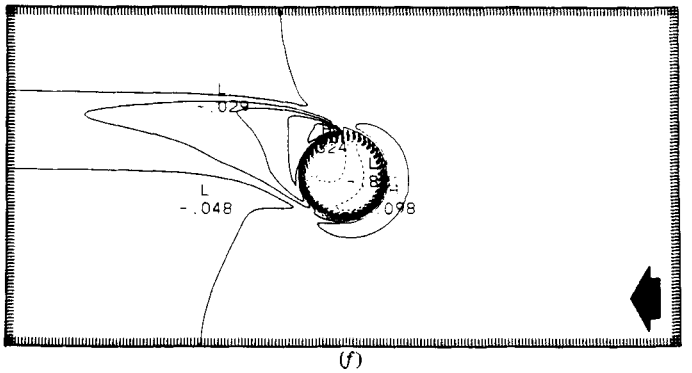

(*f*)

FIGURE 15. Numerical experiments for a disk in westward flow simulating the respective laboratory experiments in figure 6. Dimensional parameters, all figures: $R = 2.54$ cm, $H = 3.49$ cm, $L = 21.2$ cm, $h = 0.88$ cm, $\omega = 1.0$ rad/s, $\alpha = 0.0536$. Dimensionless parameters, all figures: $E = 7.4 \times 10^{-4}$, $2h/H = 0.50$, $R/H = 0.73$. (a, b) $U = 0.25$ cm/s, $Ro = 4.9 \times 10^{-2}$ $(Re = 66)$, $\beta = 0.80$; (c, d) $U = 0.50$ cm/s, $Ro = 9.8 \times 10^{-2}$ $(Re = 133)$, $\beta = 0.40$; (e, f) $U = 1.00$ cm/s, $Ro = 19.6 \times 10^{-2}$ $(Re = 266)$, $\beta = 0.20$. The respective contour intervals are (a) 0.3 cm^2 s^{-1}, (b) 0.07 s^{-1}, (c) 0.6 cm^2 s^{-1}, (d) 0.08 s^{-1}, (e) 2.0 cm^2 s^{-1}, (f) 0.07 s^{-1}.

topographic stretching term as the streamline crosses the topographic feature. If one assumes that

$$\frac{\mathrm{D}Q}{\mathrm{D}t} = 0, \tag{5.8}$$

then it can be shown that, in the steady state, the potential vorticity is a function of ψ alone; i.e.

$$Q = F(\psi) \tag{5.9}$$

or

$$\nabla^2\psi - \frac{4\omega}{H}\delta(x, y) + \frac{4\omega \tan\alpha}{H} y = F(\psi). \tag{5.10}$$

Far upstream, the first two terms are negligible, so the function F is fixed by the upstream conditions, i.e.

$$F(\psi) = -\frac{4\omega \tan\alpha}{HU}\psi + \frac{4\omega \tan\alpha}{2H} y_0. \tag{5.11}$$

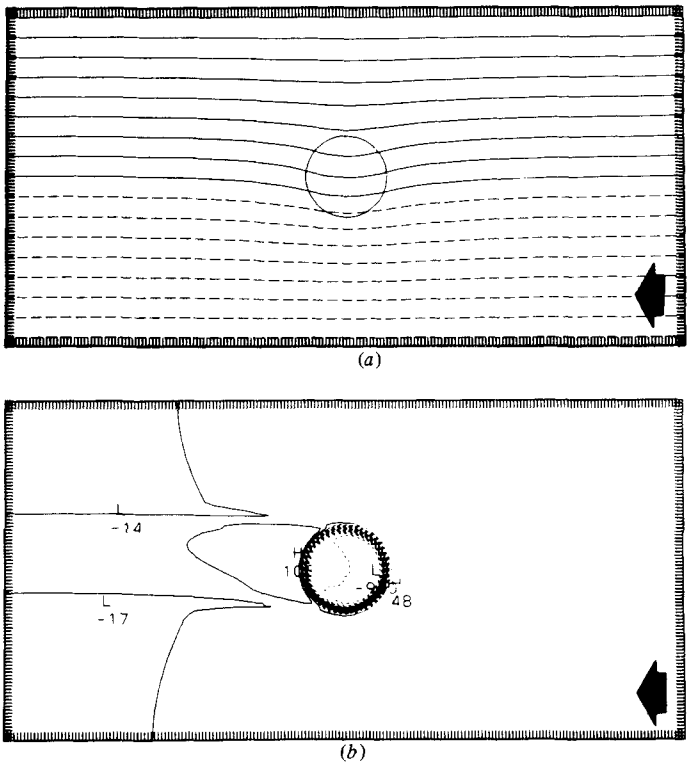

FIGURE 16. Numerical experiment for a disk in westward flow extending those runs in figure 15 to a higher Rossby number. Dimensionless parameters: $E = 7.4 \times 10^{-4}$, $2h/H = 0.50$, $R/H = 0.73$, $Ro = 0.78$ ($Re = 1054$), $\beta = 0.05$. (*a*) Stream function (contour interval 10.0 cm^2 s^{-1}); (*b*) vorticity (contour interval 0.06 s^{-1}).

Accordingly, the flow near to the obstacle must obey the equation

$$\nabla^2\psi + \frac{4\tan\alpha}{HU}\psi = \frac{4\omega}{H}\delta(x,y) + \frac{4\delta\tan\alpha}{H}\left(\frac{y_0}{2} - y\right). \tag{5.12}$$

For westward flow ($U < 0$) this is simply a Helmholtz equation, which can be easily solved by fast-Fourier-transform techniques. This gives us another limiting case, one in which the flow is frictionless but one in which the role of the obstacle in disturbing the flow can be readily investigated. (Note, however, that eastward flow (i.e. $U > 0$) leads to a wavelike equation and the disturbance associated with solutions to this equation will be felt far from the obstacle.) Neither laboratory nor numerical experiments were conducted on this problem.

In addition to trying a variety of inflow and outflow boundary conditions, two other kinds of supplementary numerical experiments were carried out. The first was to vary the domain size, that is the width and length of the channel, while keeping the grid size and obstacle the same. Figure 17 shows the result of carrying out calculations for the same obstacle and other physical parameters as that in figures 14(*a*, *b*) but in a domain extended to 63.6×42.4 cm (i.e. 300×200 grid points). The stream function and vorticity show nearly identical behaviour near the disk (note that the contour interval in figure 17(*a*) is a factor of two greater than in figure 14(*a*)). The far field is, however, somewhat altered, as the topographic Rossby wave is less constrained in the larger basin. These far-field effects have little influence on the flow

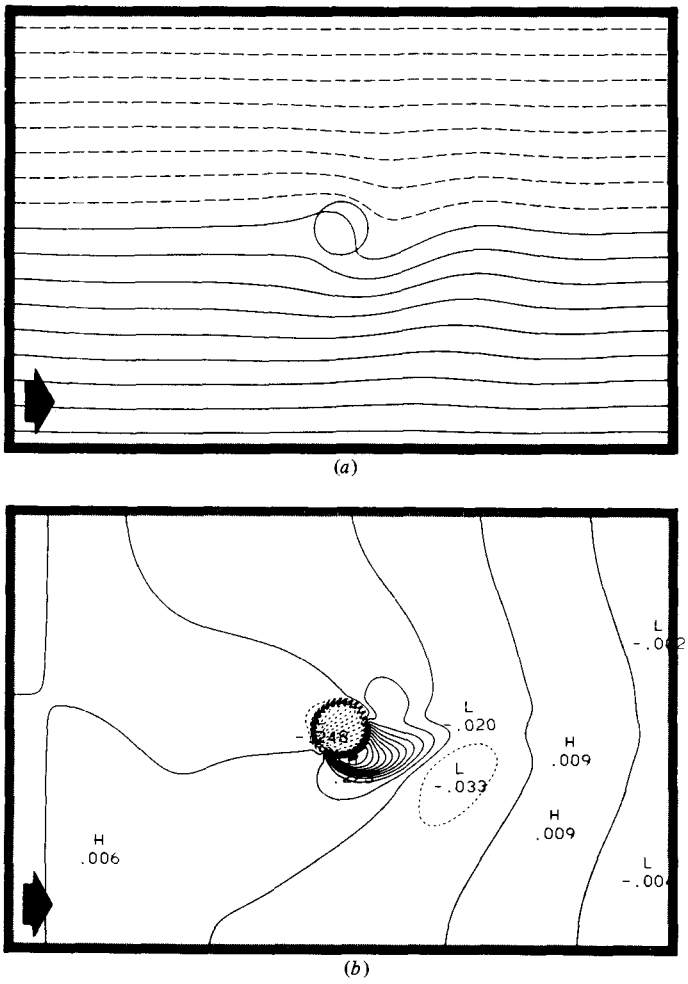

FIGURE 17. A numerical experiment for the same physical problem as in figures 14(*a*, *b*) but in a domain 1.5 times as long and 2 times as wide (i.e. 63.6×42.4 cm); $R = 2.54$ cm, $H = 3.49$ cm, $L = 42.4$ cm, $\omega = 0.5$ rad/s, $U = 0.25$ cm/s, $\alpha = 0.0536$, $h = 0.44$ cm. (*a*) Stream function (contour interval 0.6 cm^2/s); (*b*) vorticity (contour interval 0.02 s^{-1}).

near the obstacle, so the smaller, more-cost-effective basin was chosen for most of the numerical experiments. If one wanted to study the far-field behaviour, however, the larger domain (and ones even larger yet) would have to be used. It should be noted that Stevenson & Janowitz (1977) considered the far field in eastward beta-plane flow past shallow topography for the case when Ekman suction is present. Their general far-field results were qualitatively similar to those obtained in the present numerical studies.

A discussion of numerical simulations such as these requires some remarks about resolution and accuracy. In the experiments discussed above, a grid interval of 0.212 cm was used throughout. Figure 18 shows two experiments, duplicating the figure 14(*a*, *b*) results, but with *double* ($\Delta x = 0.106$ cm) and *half* ($\Delta x = 0.424$ cm) the resolution (other factors being kept constant) to assess the accuracy of the solutions. It was found that the coarsest resolution (figures 18*c*, *d*) showed differences from the finest resolution (figures 18*a*, *b*) in the vorticity maxima and minima of 12 % or less,

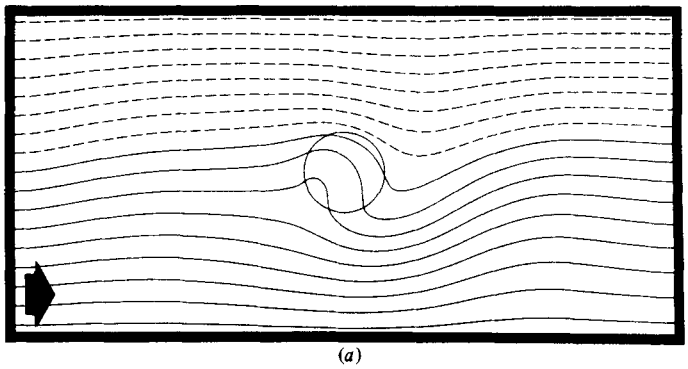

(a)

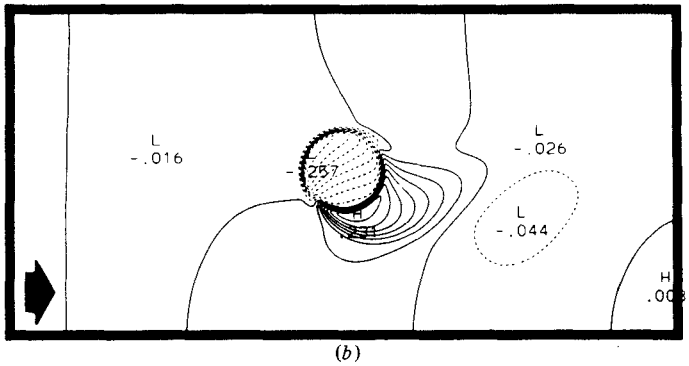

(b)

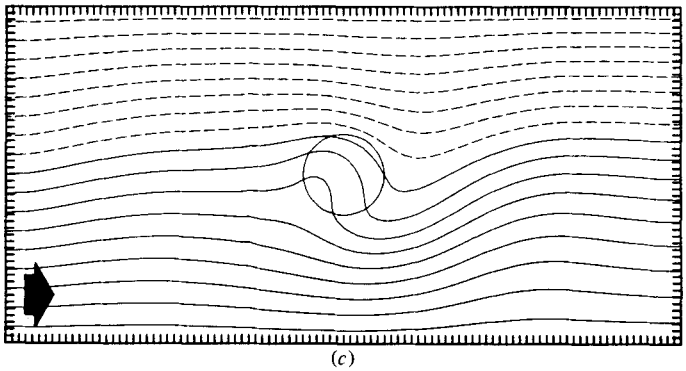

(c)

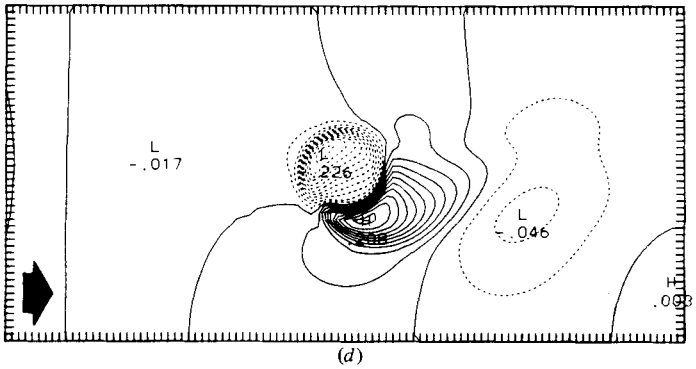

(d)

FIGURE 18. Two numerical experiments for the same physical problem as in figures 14(*a*, *b*) but with twice the resolution (*a*, *b*) and with half the resolution (*c*, *d*). (*a*, *c*) Stream functions; (*b*, *d*) vorticity fields. The contour intervals are the same as in figures 14(*a*, *b*).

while the intermediate resolution (figures 14*a*, *b*) differed from the fine-resolution case by about 4% in these measures. The streamline patterns are virtually identical, and none of these errors is large enough to change in any way the above discussion of results.

Finally, although the computational cost in reproducing numerically the laboratory results shown in figures 8–11 would be exorbitant, a few comparisons of U_s as determined in laboratory and numerical experiments is possible. The numerical experiments shown in figure 15 have common parameters with the plots in figure 9. The numerical experiments show U_s increasing faster, as a function of Ro, than U_s measured in the laboratory. This discrepancy is not resolved, but high-resolution calculations and calculations with a variety of sidewall widths W_0 show that it is not due to finite-difference numerical errors, to domain size, or to the finite width of the sidewalls of the disk in the numerical model (versus vertical sidewalls in the laboratory). The differences are most likely due to other physical differences in the two (numerical and laboratory) flows, i.e. the quasigeostrophic two-dimensional flow approximation of the model compared with the real, possibly three-dimensional, fluid flow in the laboratory.

6. Summary

A series of laboratory experiments on the flow past disks and cylindrical depressions utilizing a rotating water channel has been conducted. Coupled with these laboratory studies, numerical integrations of the quasigeostrophic potential-vorticity equation for steep-sloped topographic features have been carried out in order to simulate the laboratory experiments. The laboratory and numerical experiments are found to be in good agreement. The numerical experiments have been performed using rather modest computing resources and were found to be helpful in elucidating the dynamics of the laboratory studies as well as providing a capability for extending the parameter range of the laboratory runs.

The authors would like to thank Mr Michael Kmetz for his efforts in the conduct of the laboratory portions of this study. This work was supported by the Atmospheric Sciences Section of the National Science Foundation under Grant ATM 7905933. The numerical calculations were carried out at the National Center for Atmospheric Research, which is also funded by the National Science Foundation.

REFERENCES

ARAKAWA, A. 1966 Computational design for long term numerical integration of the equations of fluid motion: two-dimensional incompressible flow. Part I. *J. Comp. Phys.* **1**, 119–143.

BOYER, D. L. & DAVIES. P. A. 1982 Flow past a circular cylinder on a beta-plane. *Phil. Trans. R. Soc. Lond.* A **306**, 533–556.

HOLLAND, W. R. 1978 The role of mesoscale eddies in the general circulation of the ocean: numerical experiments using a wind-driven quasi-geostrophic model. *J. Phys. Oceanogr.* **8**, 363–392.

PEDLOSKY, J. 1979 *Geophysical Fluid Dynamics*. Springer.

STEVENSON, J. W. & JANOWITZ, G. S. 1977 The effect of Ekman suction on a flow over a shallow topography in the beta-plane. *Dyn. Atmos. Oceans* **1**, 225–239.